nature electronics

SUPPLEMENTARY INFORMATION

https://doi.org/10.1038/s41928-019-0304-4

In the format provided by the authors and unedited.

Three-dimensional curvy electronics created using conformal additive stamp printing

Kyoseung Sim[1], Song Chen[1], Zhengwei Li[2], Zhoulyu Rao[3], Jingshen Liu[4], Yuntao Lu[3], Seonmin Jang[3], Faheem Ershad[5], Ji Chen[4], Jianliang Xiao[2] and Cunjiang Yu[1,3,4,5,6]★

[1]Department of Mechanical Engineering, University of Houston, Houston, TX, USA. [2]Department of Mechanical Engineering, University of Colorado, Boulder, CO, USA. [3]Materials Science and Engineering Program, University of Houston, Houston, TX, USA. [4]Department of Electrical and Computer Engineering, University of Houston, Houston, TX, USA. [5]Department of Biomedical Engineering, University of Houston, Houston, TX, USA. [6]Texas Center for Superconductivity, University of Houston, Houston, TX, USA. *e-mail: cyu15@uh.edu

Supplementary Note

1. Detailed comparison between the CAS printing and pad printing

Although the operation procedures of the CAS printing have many similarities to those of pad printing, there are also many key differences, which differentiate one to the other, as described in the following and also listed in Supplementary Table 1.

1) Their primary purposes and capabilities are quite different, as listed below and also summarized in the table.
2) The associated mechanics of pad printing and CAS printing are different. Our CAS printing uses balloon stamp with a thin wall around 20 μm thick. It is noted that the original thickness of balloon stamp is around 500 μm thick; after inflation, the volume increased by 125 times and the thickness of the wafer reduced by 25 times. During the CAS printing steps, the balloon stamp experiences tensile strain, therefore thin Si elements or electronics can be printed without wrinkling or fracture.

   However, the pad printing uses a relatively thick rubber pad with wall thickness of a few mm. Because of such thick pad, during pad printing, the pad will endure compressive strain instead of tensile, especially when targeting to print onto objects with large curvatures, like those demonstrated in our study. Such compressive strain with thin Si elements or electronics will be detrimental to electronics. Once compressive strain is associated with the pad, the Si elements either delaminate from the pad, or wrinkle, or fracture, depending on the surface adhesion strength, the thickness of the Si, the planar geometry of the Si, the relative thickness ratio between the Si elements and pad. Rigid Si on an mm thick rubber under compression have been extensively studied by Rogers, Huang, and many others[1-5].

3) Pad printing has been primarily employed for solvent based or wet ink. For wet inks, pad printing could operate nicely with the compressive strain on the pad, since the ink is more tolerable to deformation. However, CAS printing is primarily designed to focus on printing rigid objects.

   Because of the wet nature of the ink, pad printing ends up with residuals after printing. However, CAS printing does not have those residuals of inks, if the competing mechanics works properly.

4) If multiple materials printing is needed, pad printing requires multiple pads, because the pads are contaminated after each printing procedure. However, CAS printing can perform multiple materials printing with a single balloon stamp, as the residual is not an issue, as discussed in 4). CAS printing multiple materials is not demonstrated in this study, but our group has been investigate this and will report the results in the near future.

5) The pad printing typically printing inks with thickness in the range of a few μm. On the other hand, CAS printing can printing inks with a much wider range, from nm to mm or even thick, if the interfacial competing mechanics is rationally designed.

6) The resolution (planar geometry) of the inks are different. For the pad printing, the ink is typically prepared based on gravure printing, therefore the resolution of the ink is mainly depend on the gravure printing with resolution of a few mils, i.e. tens to hundreds μm. For the CAS printing, the ink is pre-fabricated based on microfabrication, the resolution can be easily achieved at μm or sub-micron.

7) The electronics device performance, based upon the pad printing (if it is adopted), is much lower than that based on the CAS printing. The reason is because of the materials limitation. The similar reason has been discussed in 3D printing using wet, slurry inks.

CAS printing has a clear merits is that it offers high performance electronics as it takes advantage of Si wafer technologies.

8) The adhesion between the stamp and ink is quite different for the pad printing and CAS printing. For pad printing, the properties of the wet inks play important role in the picking up and printing steps. For CAS printing, the stamp/ink adhesion strength can be modulated, for instance based on kinetics, owing to the viscoelastic properties of the coating layer used.
9) The accuracy and alignment between the stamp and ink, and also stamp and receiver substrate for both printings are quite different. Existing pad printing is hard to achieve high accuracy as the stamp is opaque. In addition, it is not quite rational that the ink resolution is low yet the alignment accuracy is high. On the other hand, CAS printing can achieve high alignment accuracy if properly equipped. For instance, my group has been developing automatic CAS printing equipment with cameras that have high accuracy similar to that of a typical photo mask aligner.
10) Pad printing required proper conditions of the environment, such as humidity, temperature because of the wet ink printing process. However, CAS printing is less sensitive as long as the competing mechanics works.

2. Finite element analysis (FEA)

A full three-dimensional finite element model (FEM) was performed to simulate the whole process of CAS printing and investigate the deformation behavior of the electronic devices including the Si pellet array, mesh, and solar cells during the CAS printing. The surface-based fluid cavity model is used to characterize the inflated balloon and provide the coupling between the deformation of the balloon and inner air pressure within the balloon. During the CAS printing, the pneumatic model based on the ideal gas is adopted to demonstrate the gas behavior within the balloon with the universal gas constant 8.314 $Jmol^{-1}K^{-1}$. The interactions between different parts are considered to be "rough" with negligible slides along the tangential direction and "hard" contact without penetration in the normal direction. Eight-node, hybrid, 3D solid elements (C3D8H) are used to discretize the geometry of balloon with initial surface area 2396 mm^2 and an initial thickness of 0.254 mm. Four-node shell elements (S4R) are used for the coating layers with an initial thickness around 0.271 mm and 40 × 40 silicon inks array. Composite shell elements S4 are used for the devices including the metal interconnects since they are very thin and have a multilayered structure.

Mooney-Rivlin hyperelastic model is used to characterize the material behavior of latex balloon with coefficients C_{10} = 0.18152 MPa, and C_{01} = 0.006506 MPa, as shown in Supplementary Fig. 43. Yeoh hyperelastic model is used for the coating layer material (Smooth-On, Clear Flex™ 50) with coefficients C_1 = 0.394 MPa, C_2 = -0.033 MPa and C_3 = 0.003 MPa, as shown in Supplementary Fig. 44. From the figures, hyperelastic model fittings agree well with the experiments. Linear elastic model is used to demonstrate the material behavior of the devices. For Si pellets array, the dimensions for each element are 100 × 100 × 1.25 μm and the spacing in between is 250 μm. The elastic modulus (E) and Poisson's ratio (μ) are E_{Si} = 130 GPa and μ_{Si} =

0.27. For the mesh, they are composed of Cu/PI (0.1 μm/1.5 μm), where E_{Cu} = 119 GPa and μ_{Cu} = 0.34 for Cu and E_{PI} = 2.5 GPa and μ_{PI} = 0.34 for PI. For the solar cells, the metal interconnects are composed of Au/PI (0.2 μm/1.5 μm), where E_{Au} = 78 GPa and μ_{Au} = 0.34. And the Si pellets (1.25 μm) are sitting on the top of PI layer (1.5 μm).

3. Sensing mechanism of Lactate sensor

The electrochemical reaction for L-lactate sensing occurs sequentially. First, the L-lactate reacts with oxygen through the lactate oxidase (LOx) catalyst, which generates pyruvate and hydrogen peroxide. The generated hydrogen peroxide is then oxidized at the electrode, which then produces electrons that can be detected as a current signal[6]. The main reaction is summarized by the two equations of reactions with LOx (S1) and the electrode (S2);

$$\text{L-lactate} + O_2 \rightarrow \text{pyruvate} + H_2O_2 \tag{S1}$$

$$H_2O_2 \rightarrow 2H^+ + O_2 + 2e^-. \tag{S2}$$

The amount of generated electrons is proportional to the concentration of L-lactate.

4. Calculation of LOD, K_M and I_{MAX} for lactate sensor.

The limit of detection (LOD), the lowest concentration that can be detected reliably, for the lactate sensor was obtained by[7]

$$LOD = \frac{3\sigma}{K} \tag{S3}$$

where σ and K are the standard deviation of the background current from PBS solution and the slope of the fitted line in Supplementary Fig. 30b, respectively. The obtained σ and K are 6.59×10^{-11} A and 9.39 μA/mM, respectively. The calculated LOD is 4.58 μM.

Supplementary Fig. 31b shows the calibration curve for a high concentration of L-lactate range (2 mM – 50 mM), which is fitted by the Michaelis-Menten Kinetic model, as follows[8]

$$I = \frac{I_{MAX} \cdot c}{K_M + c} \tag{S4}$$

where I, I_{MAX}, c, and K_M are sensing current, maximum current under saturated L-lactate condition, L-lactate concentration, and Michaelis-Menten constant, respectively, which can be extracted from Supplementary Fig. 31a with the Lineweaver-Burk equation, as follows[8,9]

$$\frac{1}{I} = \frac{K_M}{I_{MAX}} \cdot \frac{1}{c} + \frac{1}{I_{MAX}} \tag{S5}$$

The obtained slope and y-intercept from Supplementary Fig. 31a were 1.14×10^7 mM A^{-1} and 8.801×10^6 A^{-1}, respectively. Based on those value, the obtained I_{MAX}, and K_M are 113.62 nA and 1.299 mM, respectively.

Supplementary References

1 Jiang, H. *et al.* Finite deformation mechanics in buckled thin films on compliant supports. *Proc. Natl. Acad. Sci. U.S.A* **104**, 15607-15612 (2007).

2 Li, H. *et al.* Local wrinkling versus global buckling of stiff film bonded to finite-thick substrate. *Extreme Mechanics Letters* **29**, 100453 (2019).

3 Pan, K., Ni, Y., He, L. & Huang, R. Nonlinear analysis of compressed elastic thin films on elastic substrates: From wrinkling to buckle-delamination. *International Journal of Solids and Structures* **51**, 3715-3726 (2014).

4 Vella, D., Bico, J., Boudaoud, A., Roman, B. & Reis, P. M. The macroscopic delamination of thin films from elastic substrates. *Proc. Natl. Acad. Sci. U.S.A* **106**, 10901-10906 (2009).

5 Wang, S., Song, J., Kim, D.-H., Huang, Y. & Rogers, J. A. Local versus global buckling of thin films on elastomeric substrates. *Appl. Phys. Lett.* **93**, 023126 (2008).

6 Thomas, N., Lähdesmäki, I. & Parviz, B. A. A contact lens with an integrated lactate sensor. *Sens. Actuators, B* **162**, 128-134 (2012).

7 Jing, W. *et al.* Regulating the hydrothermal synthesis of ZnO nanorods to optimize the performance of spirally hierarchical structure-based glucose sensors. *RSC Adv.* **5**, 85988-85995 (2015).

8 Kausaite-Minkstimiene, A., Mazeiko, V., Ramanaviciene, A. & Ramanavicius, A. Enzymatically synthesized polyaniline layer for extension of linear detection region of amperometric glucose biosensor. *Biosens. Bioelectron.* **26**, 790-797 (2010).

9 Yu, J., Liu, S. & Ju, H. Glucose sensor for flow injection analysis of serum glucose based on immobilization of glucose oxidase in titania sol–gel membrane. *Biosens. Bioelectron.* **19**, 401-409 (2003).

Supplementary Table

Supplementary Table 1. Comparisons between pad printing and CAS printing.

		Pad Printing	CAS Printing
1	**Primary purposes**	Graphic printing	Electronics fabrication
2	**Stamp mechanics**	Compressive strain in the pad; thick wall	Tensile strain in the balloon stamp; thin wall
3	**Ink materials**	Wet, slurry ink	Dry, solid ink – Si electronics
4	**Multiple materials printing**	Multiple pad is required; the pad is contaminated after printing	A single balloon stamp is good enough; no residual
5	**Ink thickness**	~ 4 – 10 um	Wide range: from nm to mm scale
6	**Ink resolution**	~ 0.003” (75 μm)	1 μm or sub μm
7	**Device performances**	Lower performances for electronics, because of the material limitation	High performance based on traditional Si wafer technology
8	**Stamp/ink adhesion**	Not easy to modulate	Tunable based on kinetics
9	**Accuracy and alignment between the stamp and ink, stamp and receiver**	Difficult; the stamp is typically opaque	Easy; the balloon stamp is transparent and can see through and can be equipped with a cemera
10	**Environment conditions**	Sensitive	insensitive

Supplementary Figures

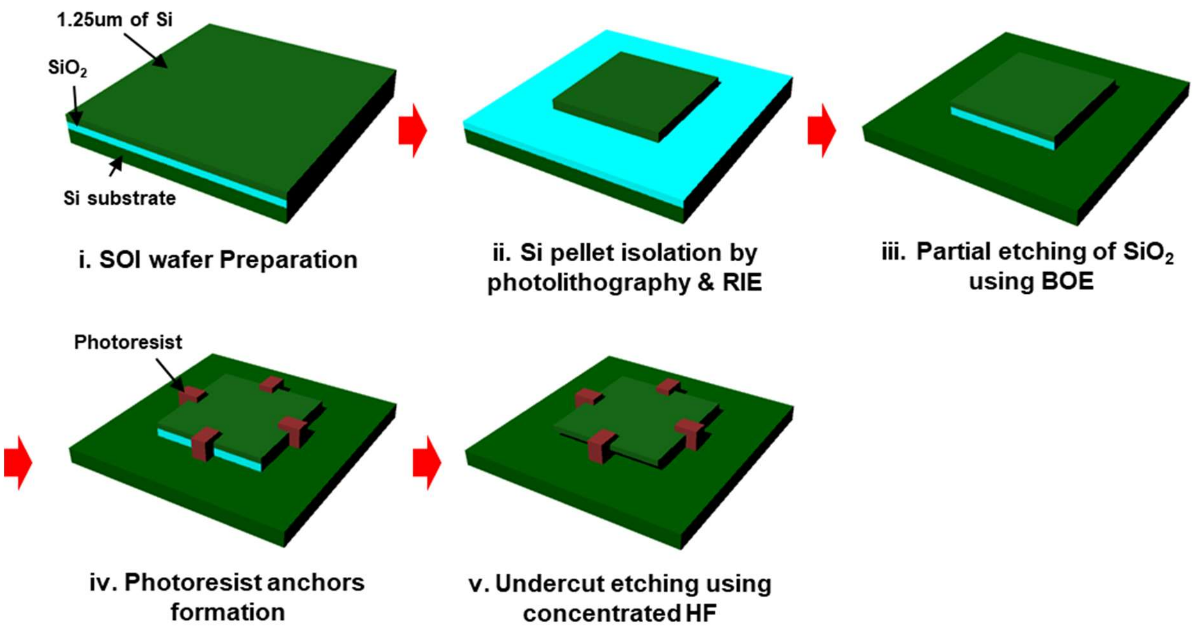

Supplementary Figure 1. Schematic procedures to fabricate a Si pellet array.

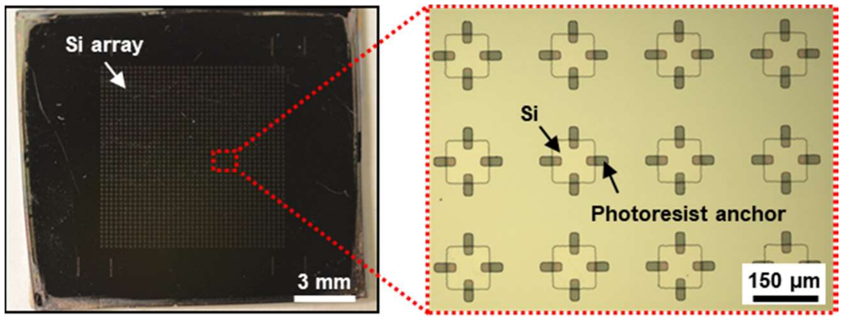

Supplementary Figure 2. Fabricated Si pellet array on an SOI wafer.

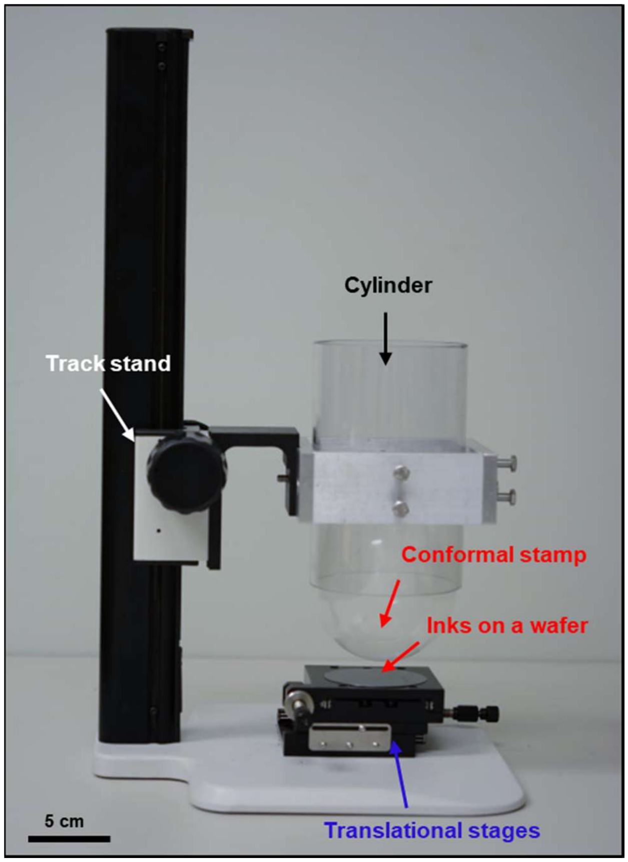

Supplementary Figure 3. An optical image of custom-made CAS printing equipment.

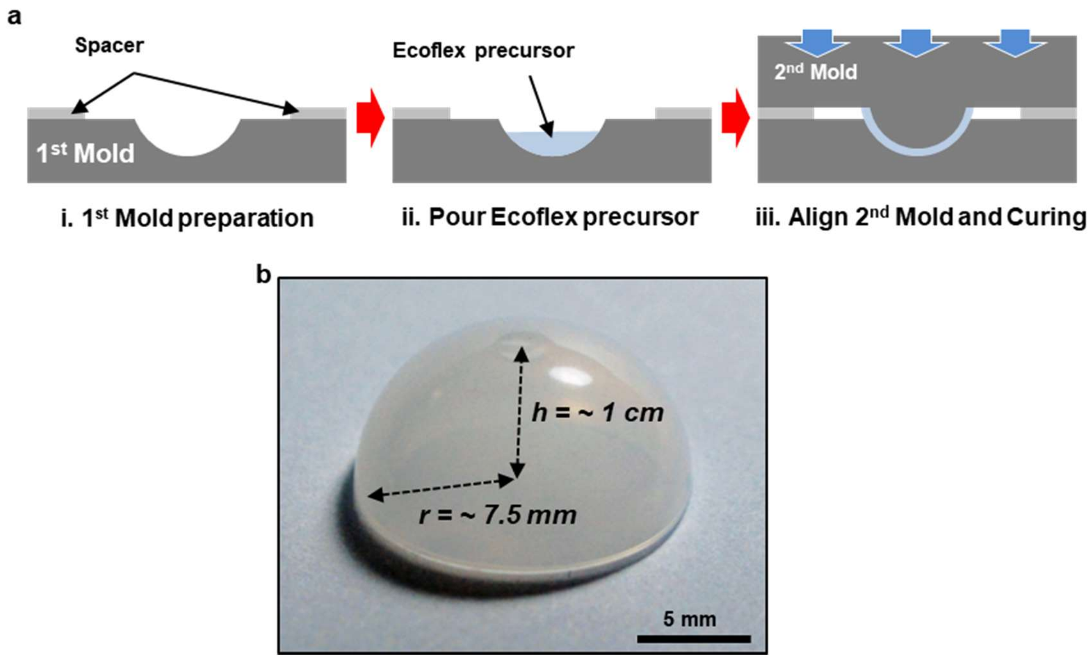

Supplementary Figure 4. Hemispherical shell preparation. **a,** Schematic illustration of hemispherical shell preparation. **b,** An optical image of a fabricated Ecoflex hemispherical shell.

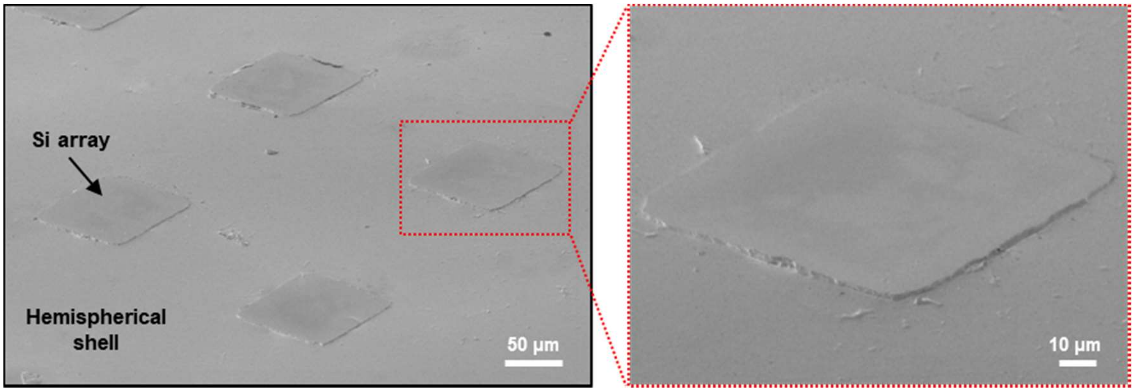

Supplementary Figure 5. SEM images of the Si array on a hemispherical shell after CAS printing

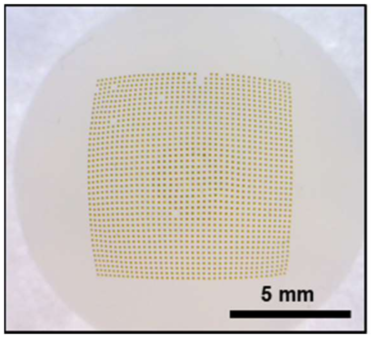

Missing Si pellets	11 out of 1521
Yield	99.28%

Supplementary Figure 6. Representative Si array on hemisphere shell after CAS printing.

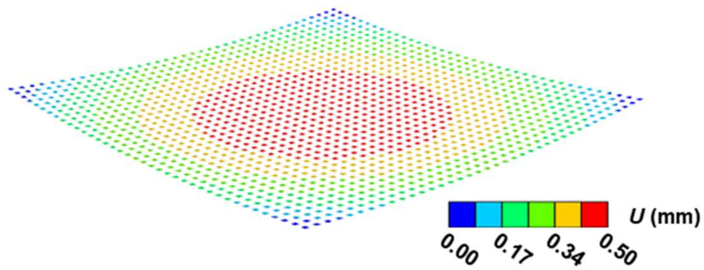

Supplementary Figure 7. Displacement contour for Si pellets array on a balloon stamp after picking up.

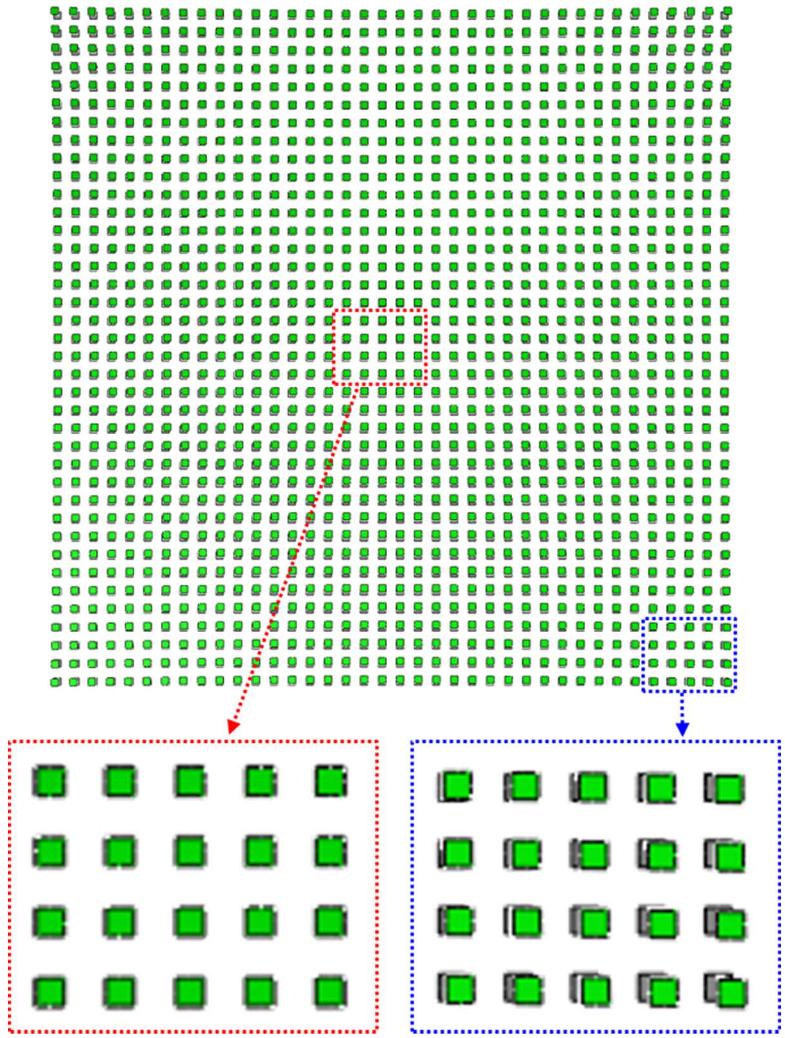

Supplementary Figure 8. FEA results of the distortion of the Si pellet array position after picking up.

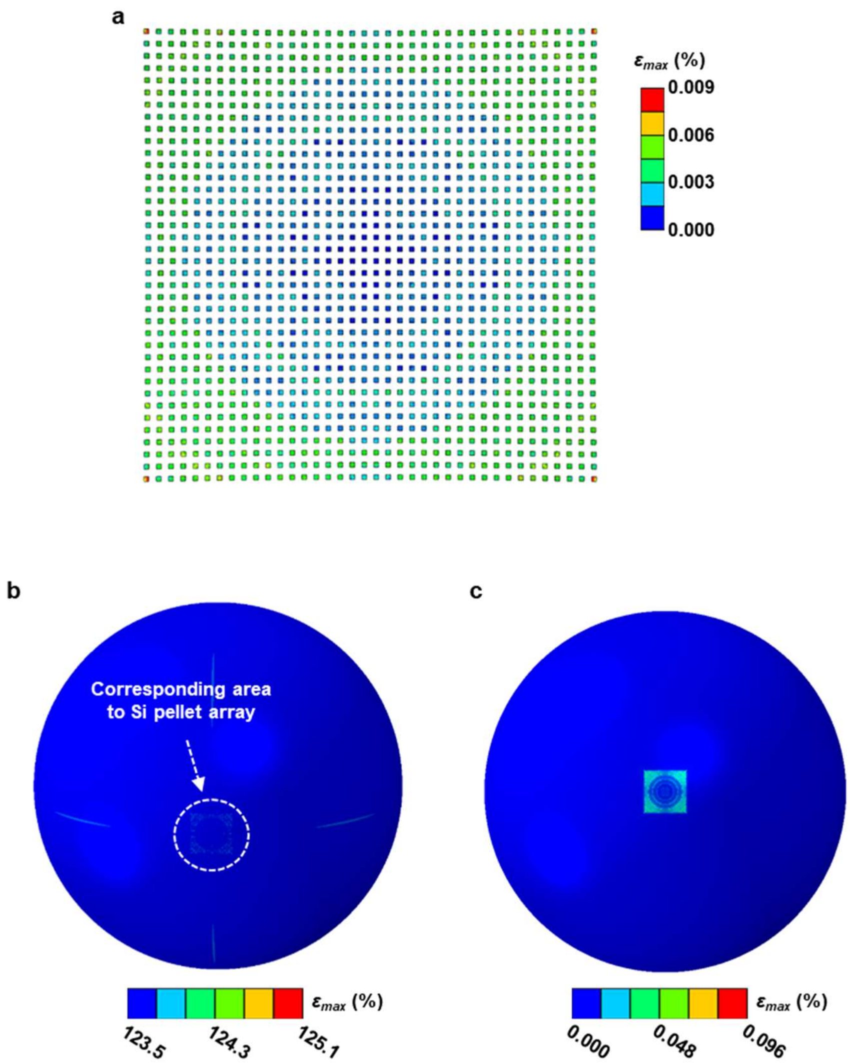

Supplementary Figure 9. The FEA results of the Si pellet array and balloon stamp after picking up. **a,** The maximum principle strain in the Si pellet array on the balloon stamp after picking up. **b-c,** The strain contours of the balloon (**b**) and Clearflex coating layer (**c**).

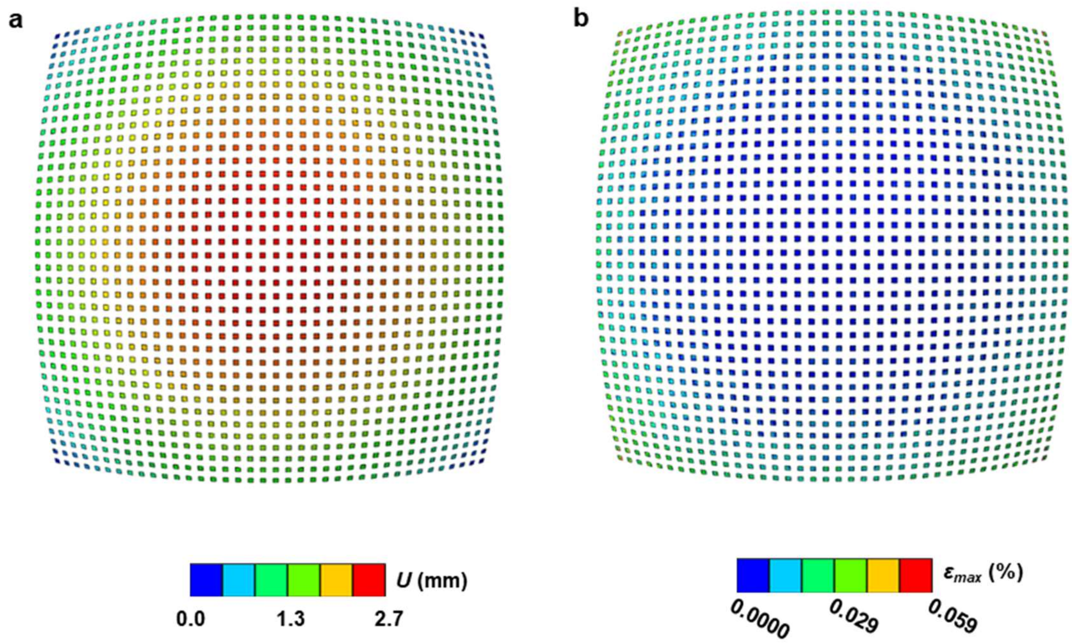

Supplementary Figure 10. The FEA results of Si pellet array on a hemispherical shell after CAS printing (Top view). **a,** The displacement contour of the Si pellet array on a hemispherical shell after CAS printing. **b,** The maximum principle strain contour of the Si pellet array on a hemispherical shell after CAS printing.

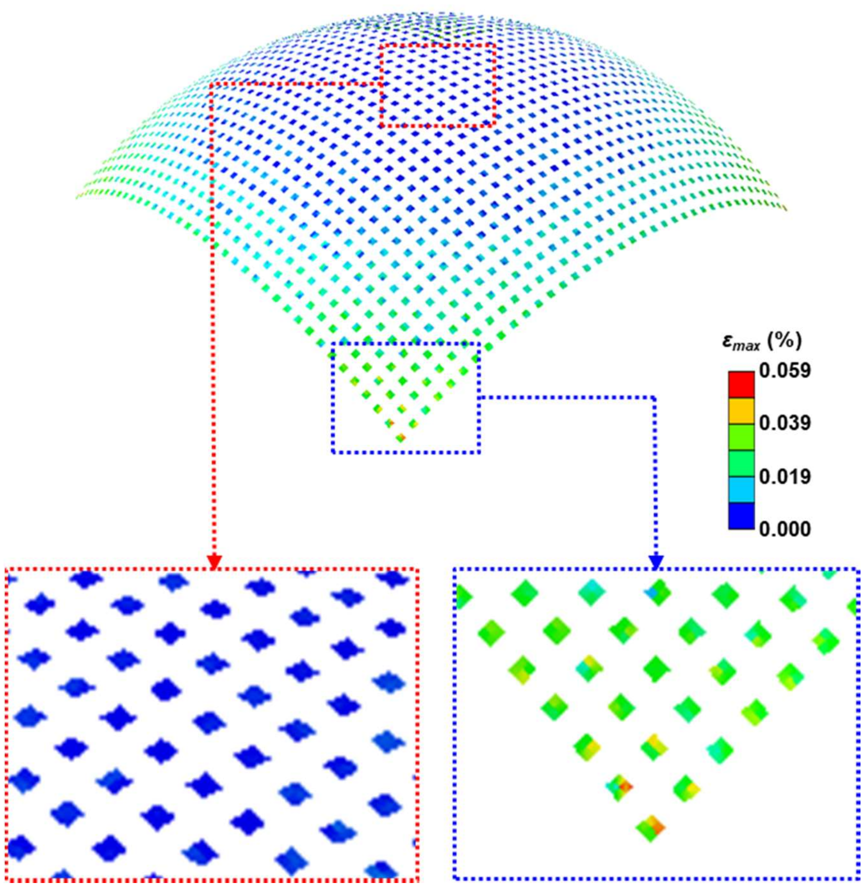

Supplementary Figure 11. The FEA results of the Si pellet array on a hemispherical shell after CAS printing in prospective view.

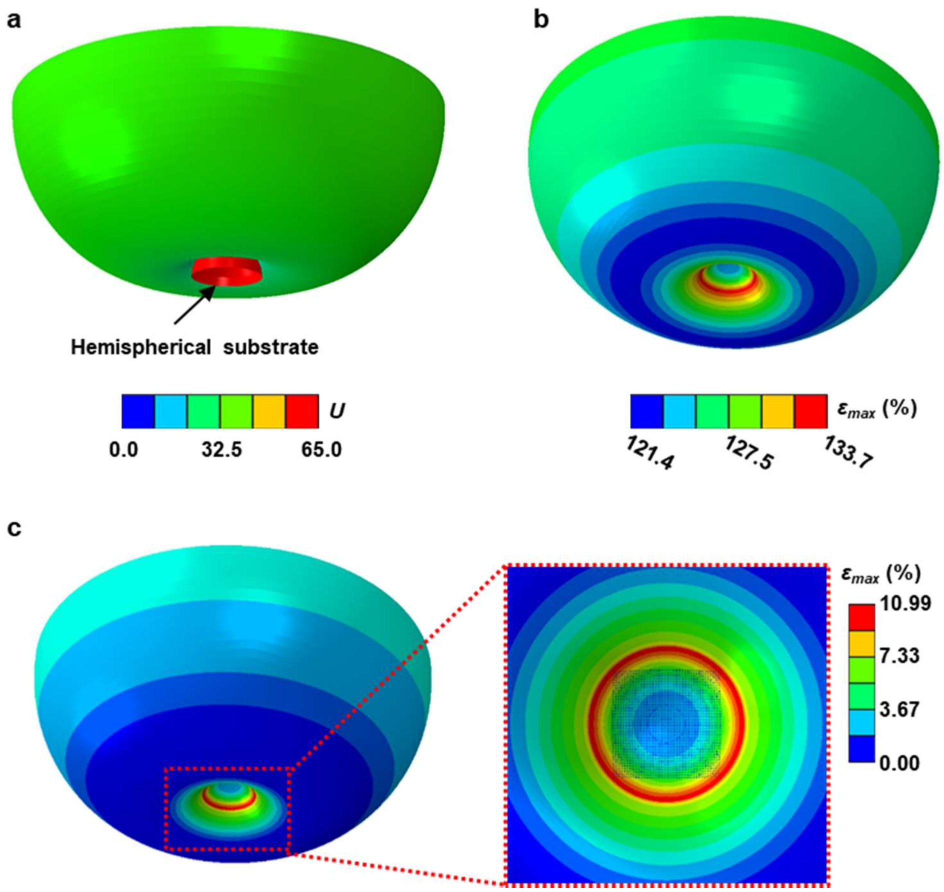

Supplementary Figure 12. The FEA results of the balloon stamp during CAS printing. **a,** The deformation of the balloon stamp during CAS printing. **b**, The maximum principle strain contour of the latex balloon during CAS printing. **c,** The maximum principle strain contour of the Clearflex coating layer during CAS printing.

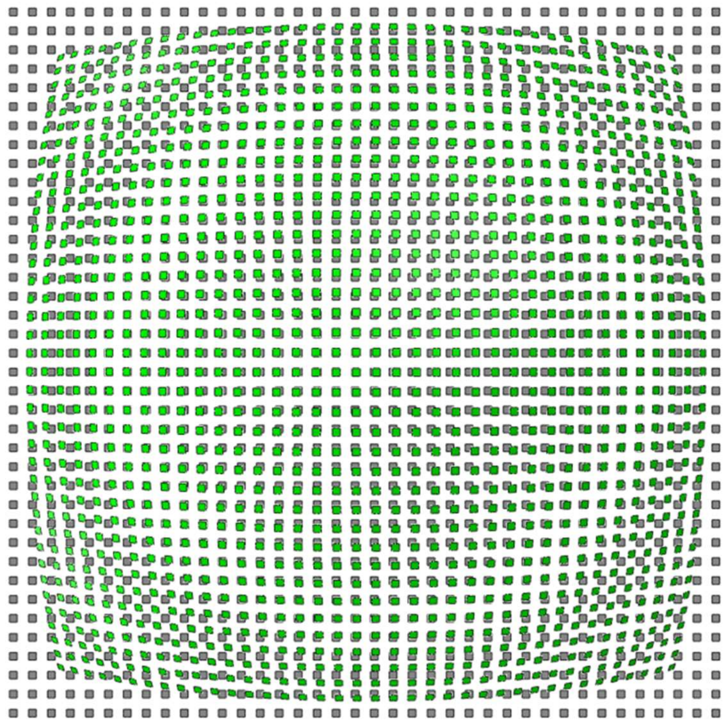

Supplementary Figure 13. The simulated position of the Si pellet array on the curvy shell (green) and on the Si wafer (gray).

a

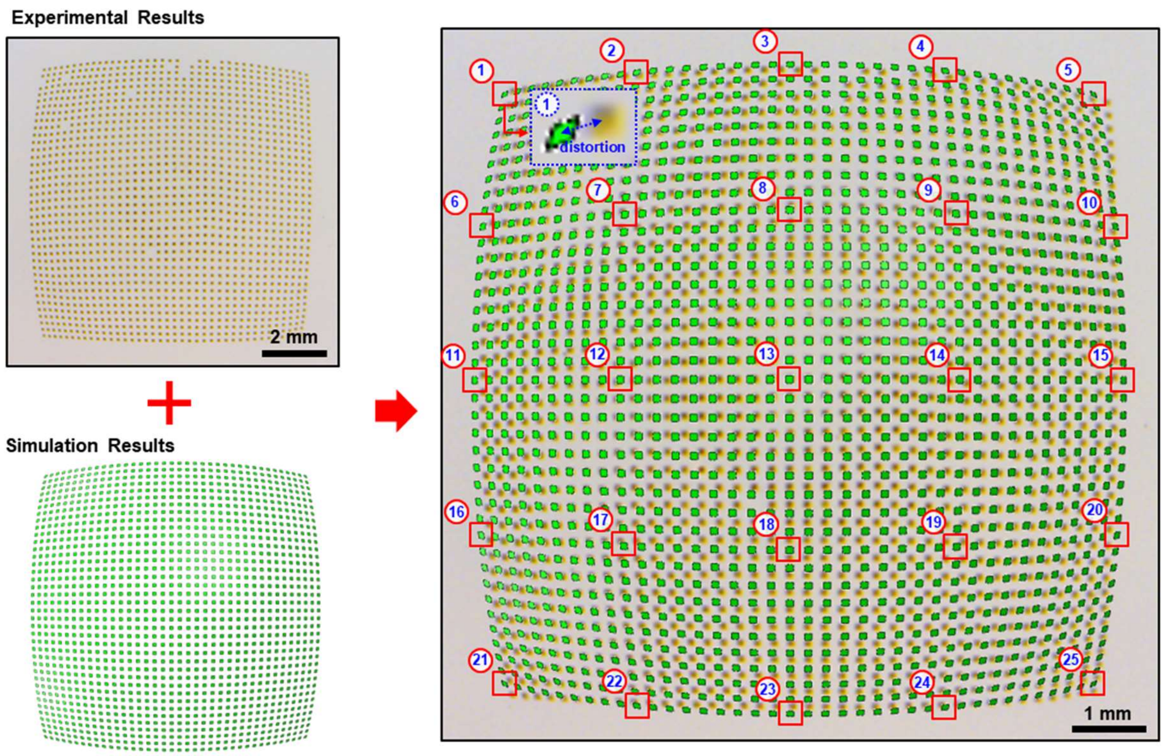

b

1	0.212 ± 0.097	**2**	0.094 ± 0.058	**3**	0.108 ± 0.074	**4**	0.186 ± 0.068	**5**	0.384 ± 0.188
6	0.091 ± 0.082	**7**	0.088 ± 0.051	**8**	0.090 ± 0.046	**9**	0.093 ± 0.038	**10**	0.231 ± 0.125
11	0.144 ± 0.065	**12**	0.095 ± 0.035	**13**	0	**14**	0.107 ± 0.072	**15**	0.194 ± 0.136
16	0.232 ± 0.082	**17**	0.141 ± 0.097	**18**	0.128 ± 0.043	**19**	0.148 ± 0.033	**20**	0.257 ± 0.145
21	0.372 ± 0.159	**22**	0.299 ± 0.107	**23**	0.242 ± 0.125	**24**	0.285 ± 0.138	**25**	0.426 ± 0.227

***Unit: mm**

Supplementary Figure 14. The distortion of Si pellet array after CAS printing comparing to simulation. a, Individual (left) and overlay (right) images of simulation and experimental results. The inset shows the magnified distortion. **b,** Distortion between experiment and simulation results. The values were obtained from 5 samples.

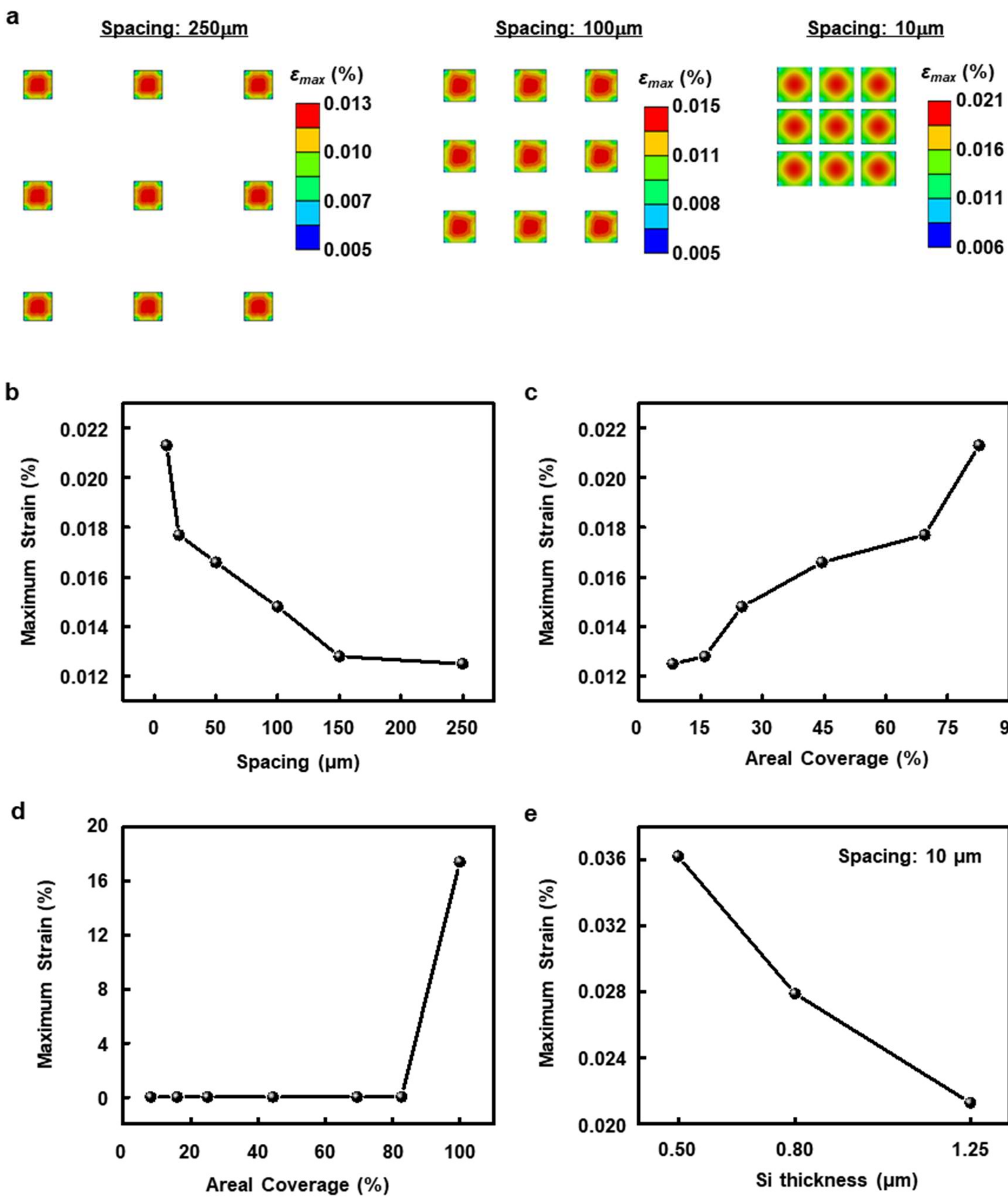

Supplementary Figure 15. The FEA results of areal coverage. a, The strain contour of 3 × 3 Si pellet array. **b,** Maximum strain of Si pellet depending on spacing. **c,** Maximum strain depending on areal coverage. **d,** Maximum strain depending on areal coverage up to 100%. **e,** Maximum strain depending on Si thickness.

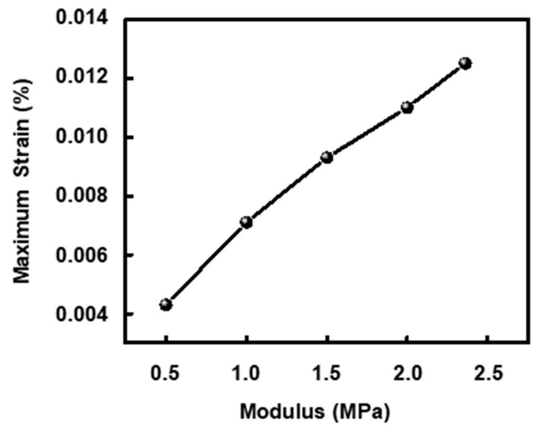

Supplementary Figure 16. Simulated maximum strain of Si pellet depending on Young's modulus of elastomeric balloon stamp.

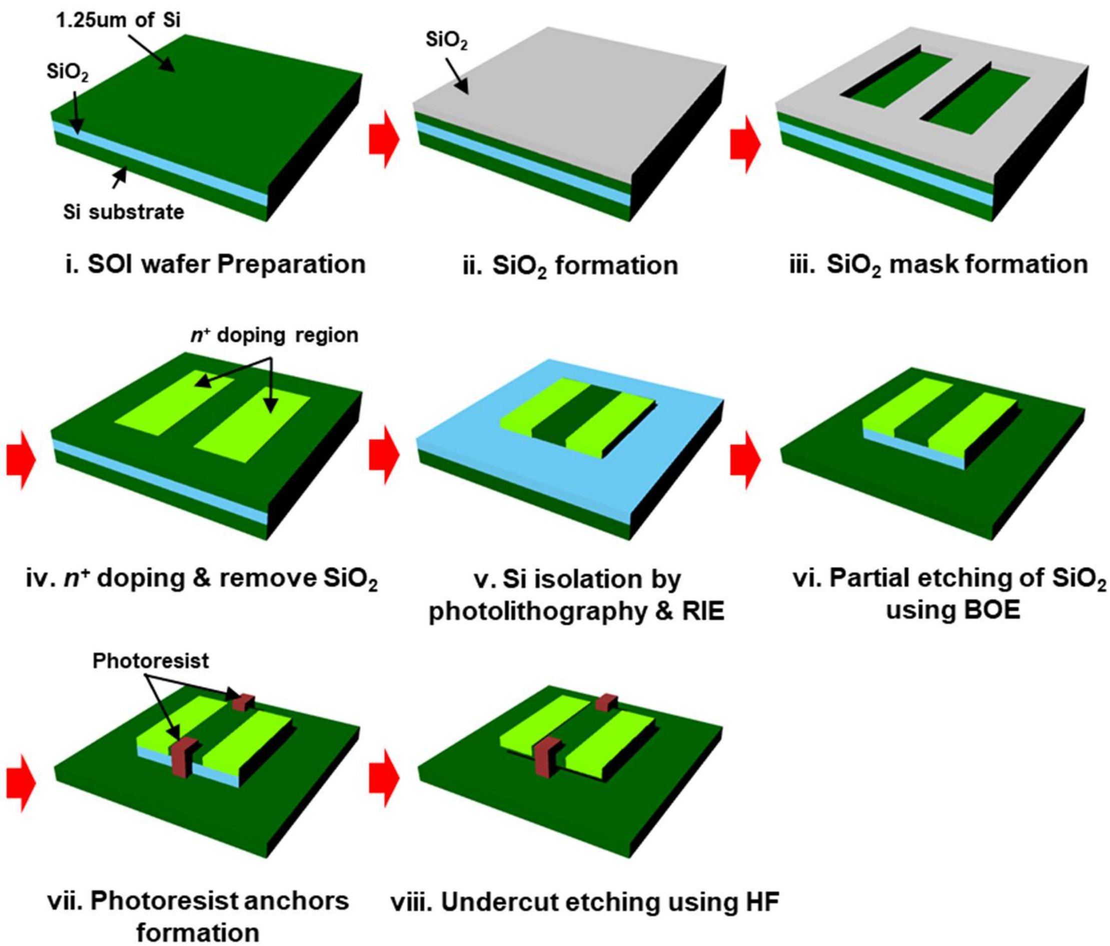

Supplementary Figure 17. Schematic procedures for Si photodetector fabrication.

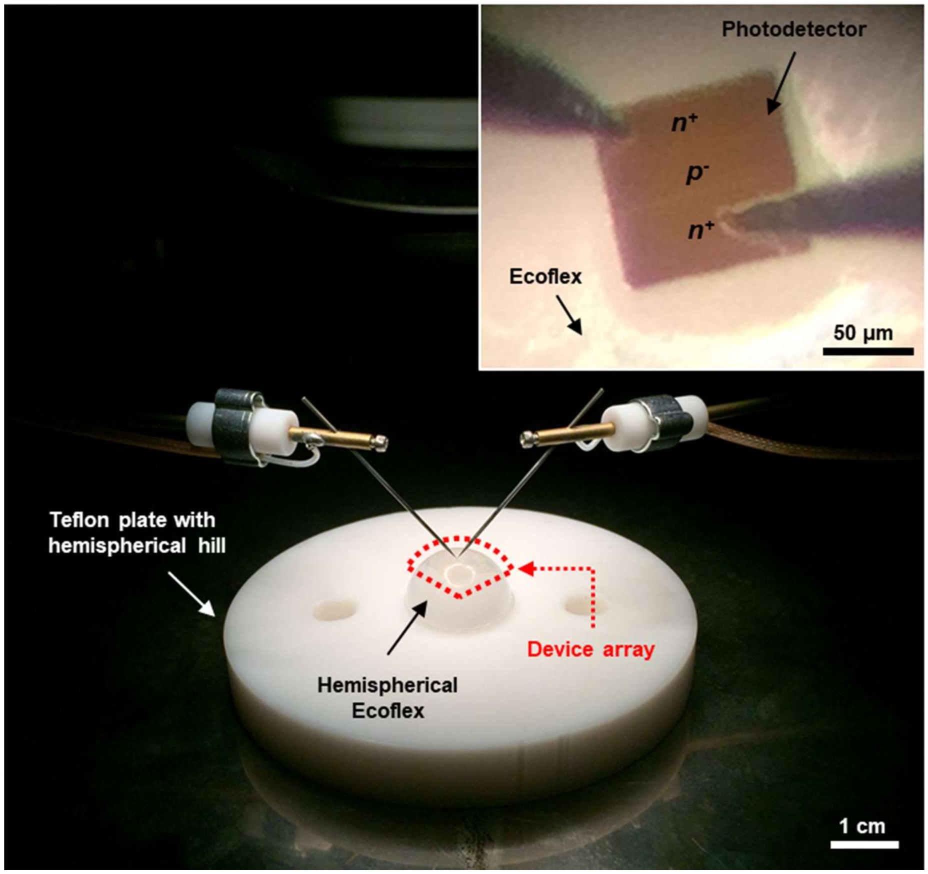

Supplementary Figure 18. Characterization setup for the hemispherical shaped photodetector array.

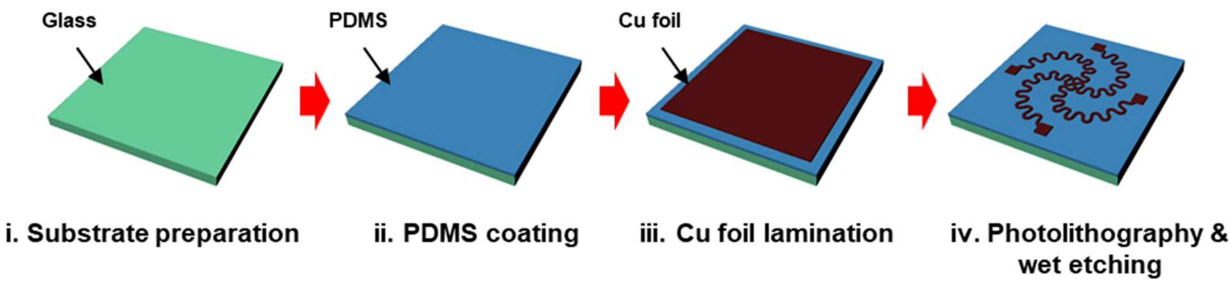

Supplementary Figure 19. Schematic procedures for the helix antenna fabrication.

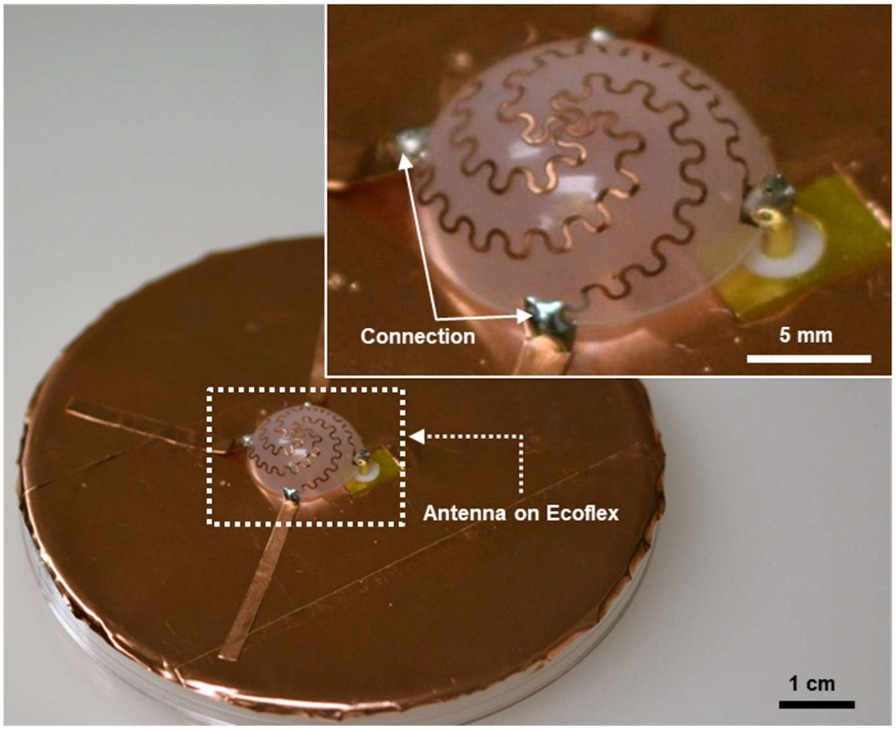

Supplementary Figure 20. Characterization setup for the Cu curvy helix antenna.

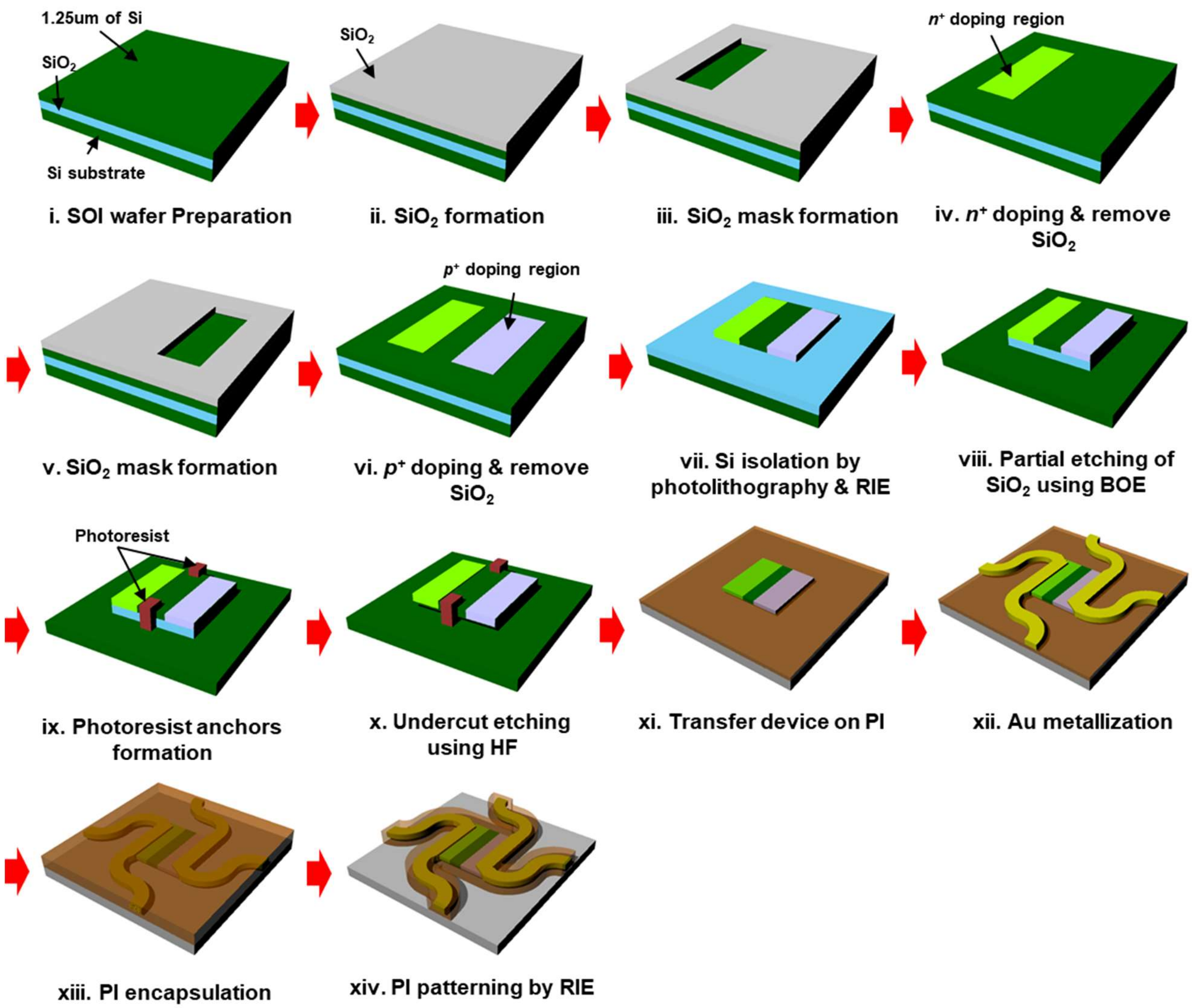

Supplementary Figure 21. Schematic procedures for Si based p-i-n solar cell fabrication.

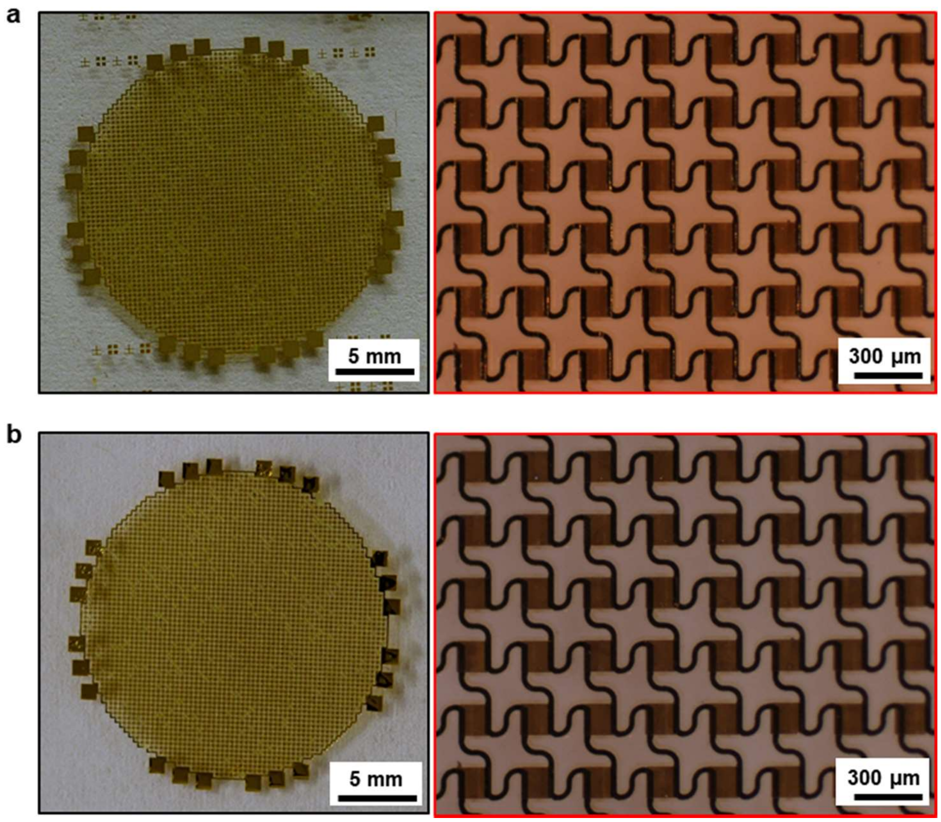

Supplementary Figure 22. Optical images of the Si based p-i-n solar cells array before releasing (**a**) and after transferring (**b**) to the temporary substrate.

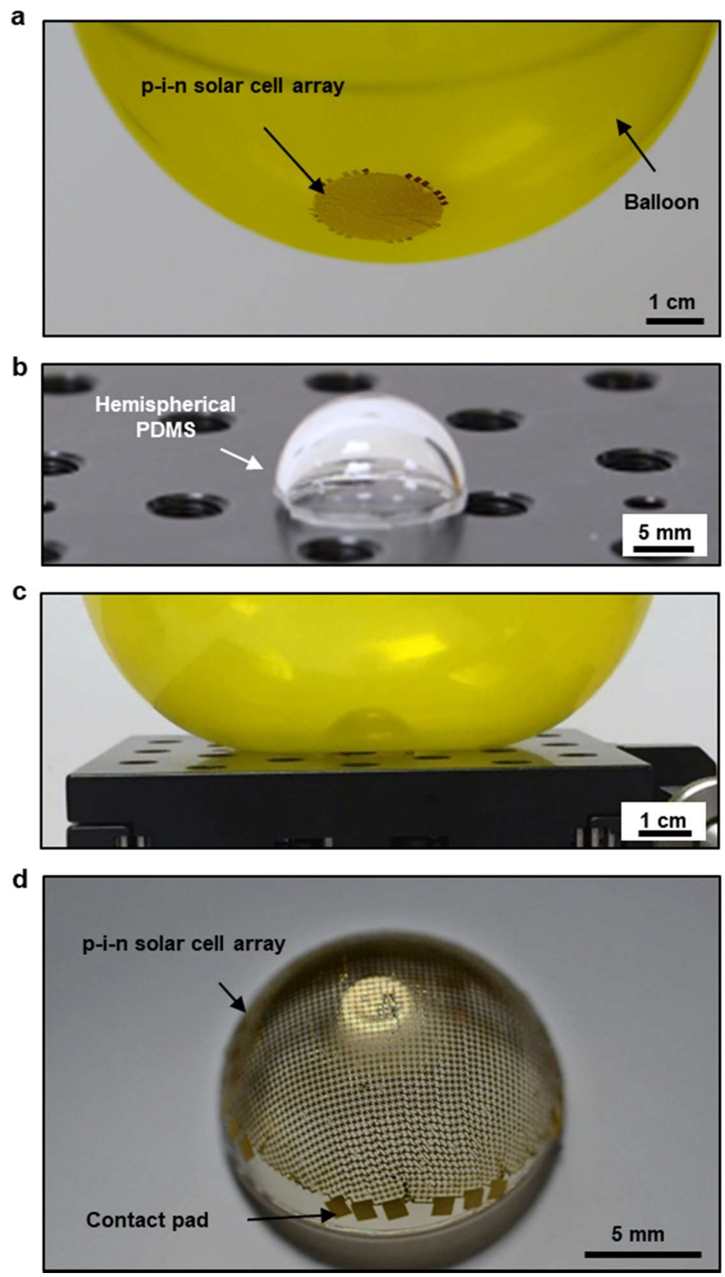

Supplementary Figure 23. CAS printing of a hemispherical solar cell. **a,** Optical image of the solar cell array on a balloon stamp. **b,** Optical image of hemispherical PDMS shell. **c,** Conformal contact between the balloon stamp with the solar cell array and hemispherical PDMS shell. **d,** Optical image of the fabricated hemispherical solar cell.

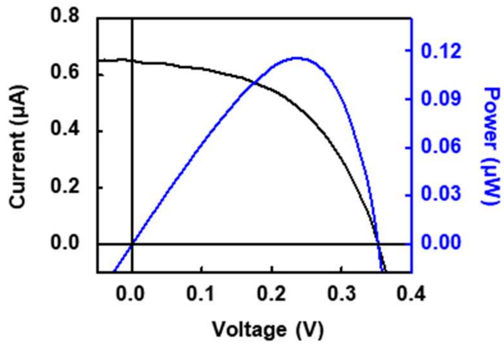

Supplementary Figure 24. The *I-V* and output power and voltage curves of one single Si p-i-n solar cell pixel.

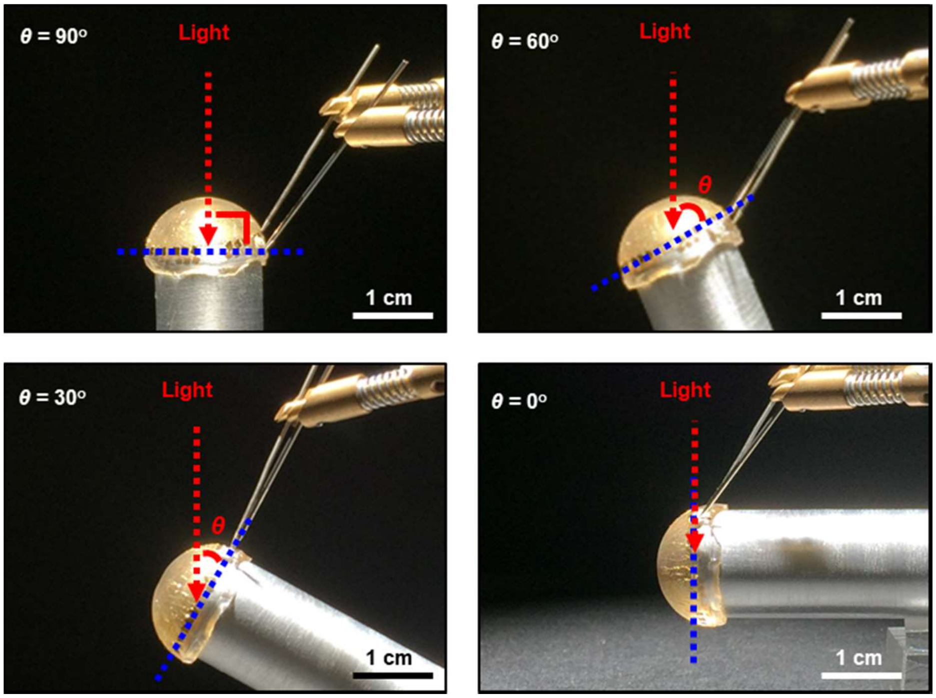

Supplementary Figure 25. Optical images of the hemispherical solar cell characterization setup.

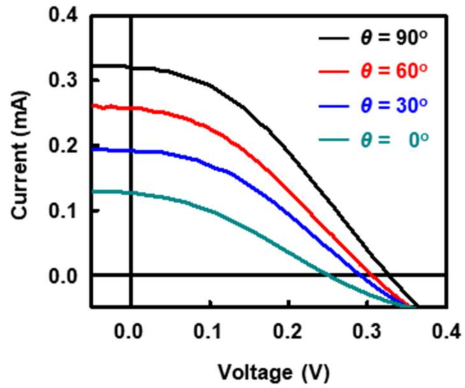

Supplementary Figure 26. The *I-V* characteristics of the Si based p-i-n solar cell array depending on the angles of incident light.

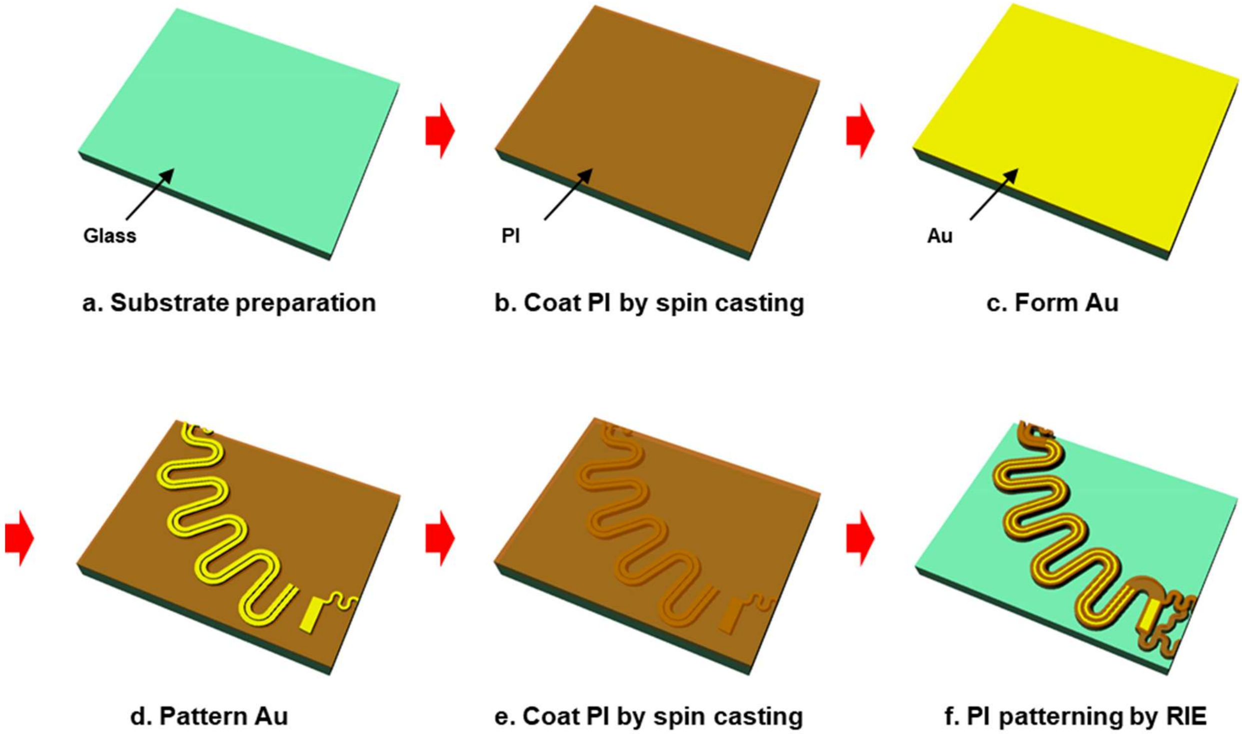

Supplementary Figure 27. Schematic procedure for electrodes for lactate sensor fabrication.

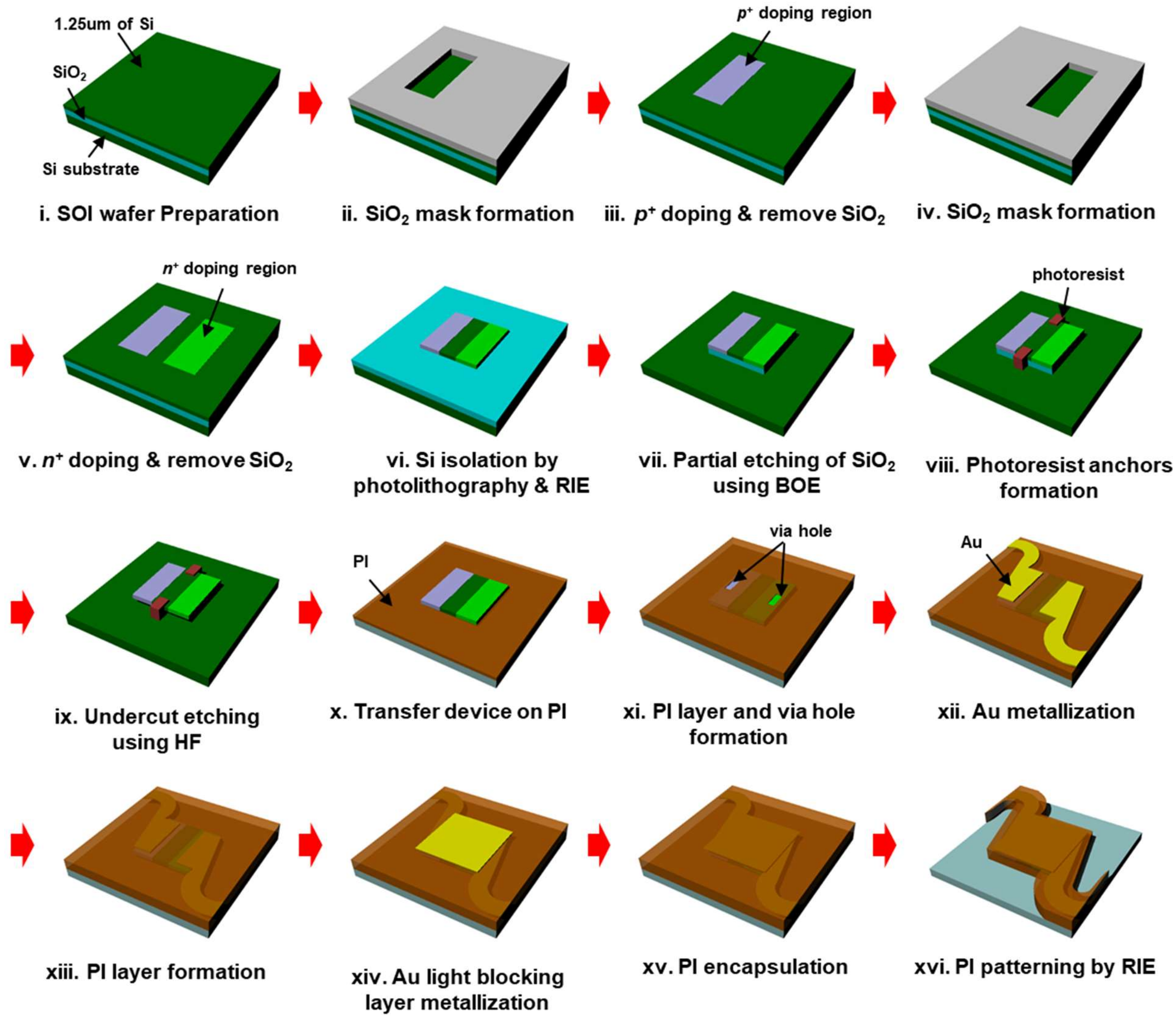

Supplementary Figure 28. Schematic procedures for the Si diode temperature sensor fabrication.

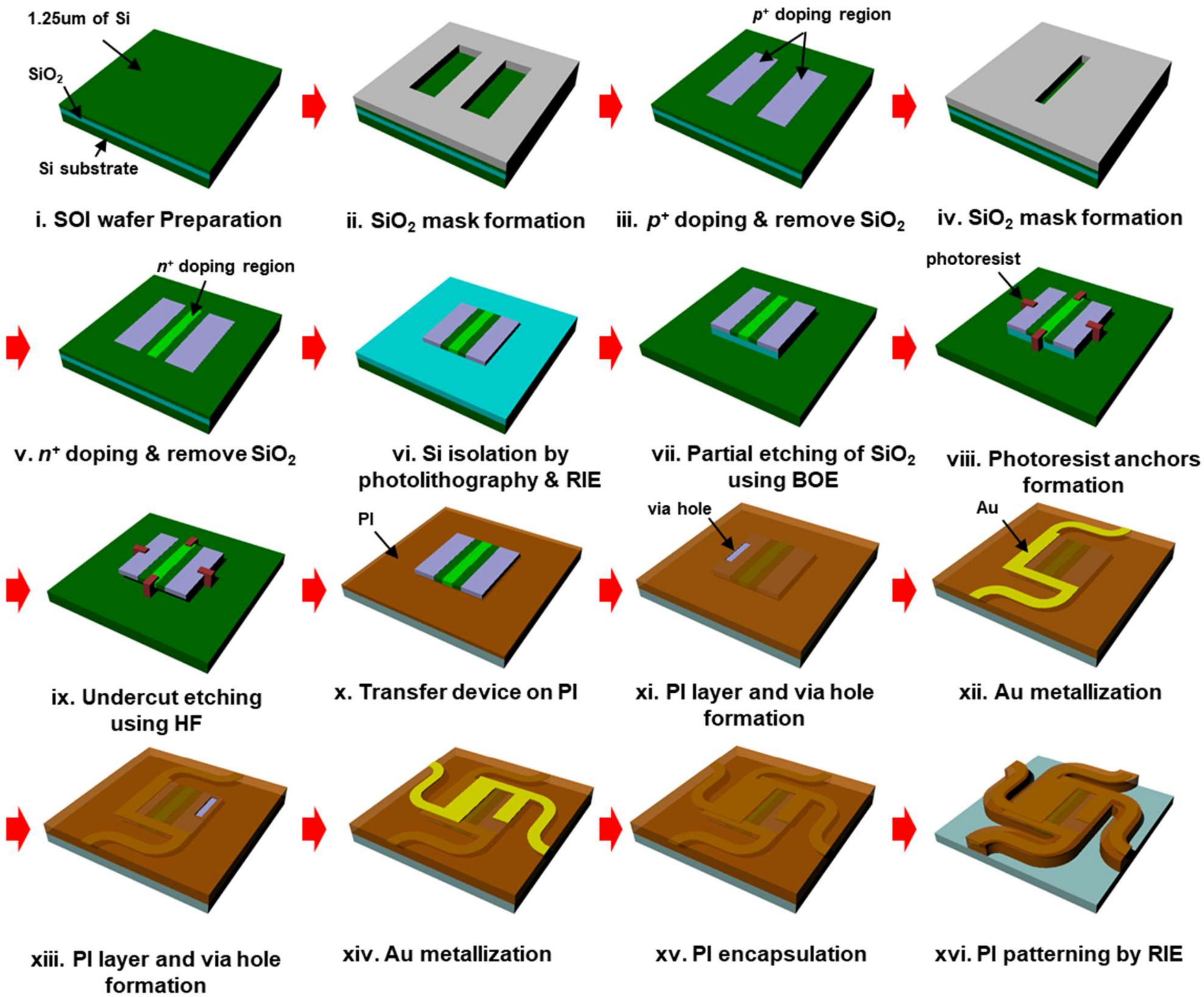

Supplementary Figure 29. Schematic procedures for the imager fabrication.

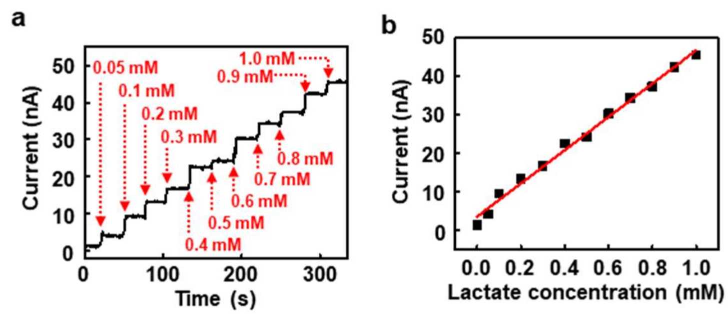

Supplementary Figure 30. Lactate sensor measurements at low L-lactate concentration range (0.05 – 1 mM). **a,** Continuous measurement under different L-lactate concentrations. **b,** Calibration curve with linear fitting curve.

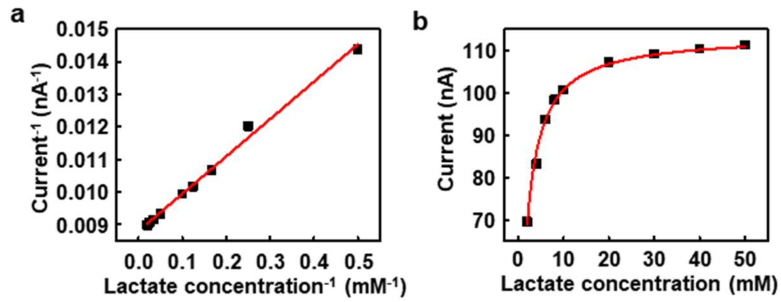

Supplementary Figure 31. Sensing current of lactate sensor at high L-lactate concentration range (2 – 50 mM). **a,** Lineweaver-Burk plot at high concentration of L-lactate. **b,** Sensing current of the lactate sensor in high concentration range with Mechaelis-Menten fitting.

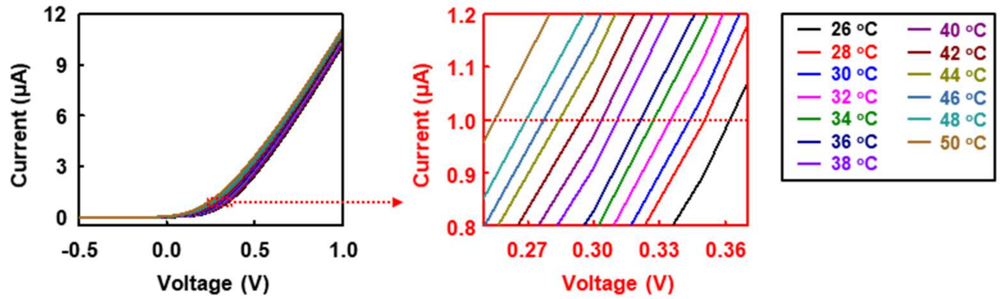

Supplementary Figure 32. I-V characteristics of the temperature sensor under different temperatures.

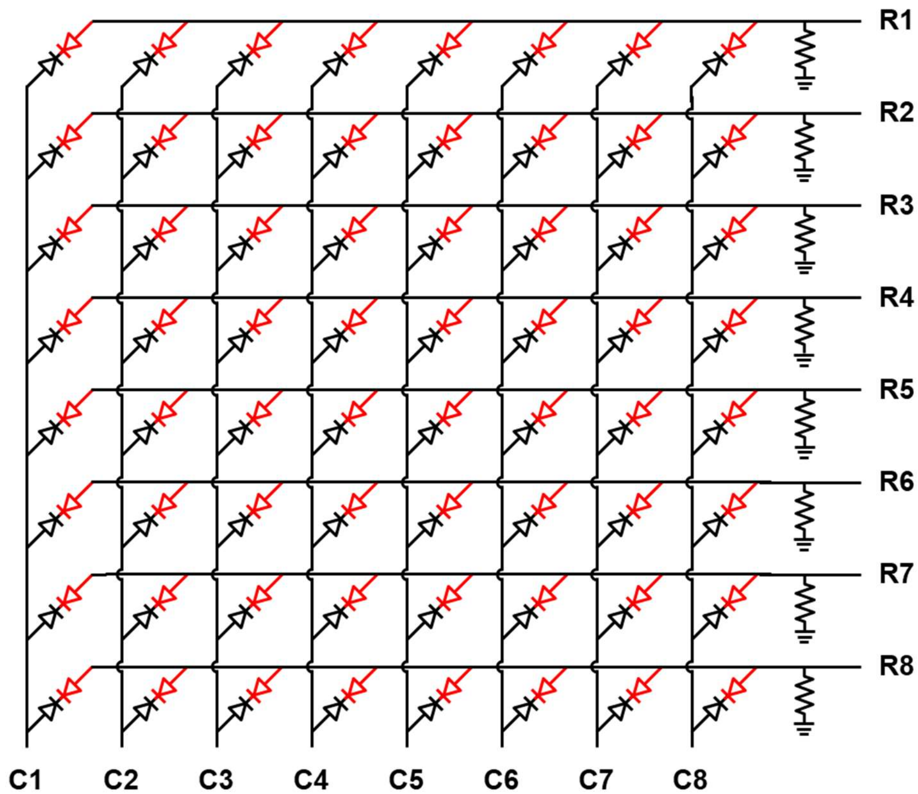

Supplementary Figure 33. Circuit diagram of the imager.

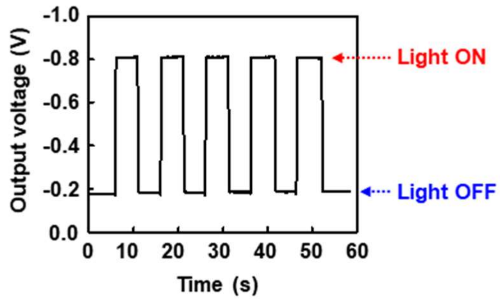

Supplementary Figure 34. Dynamic output voltage of a single pixel during repeatedly turning on and off the light.

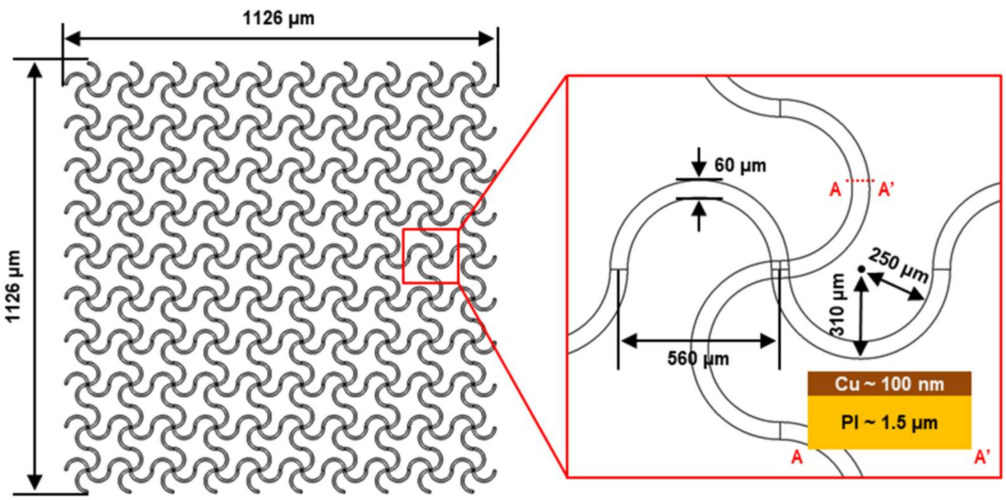

Supplementary Figure 35. The layout and geometries of the serpentine metal mesh.

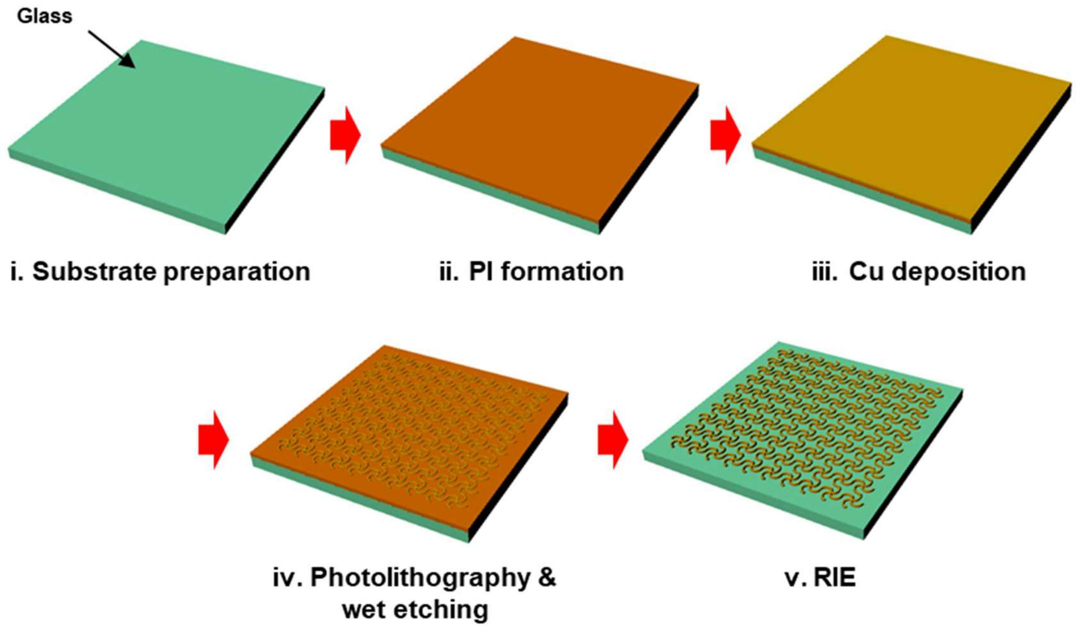

Supplementary Figure 36. Schematic procedures for the mesh fabrication.

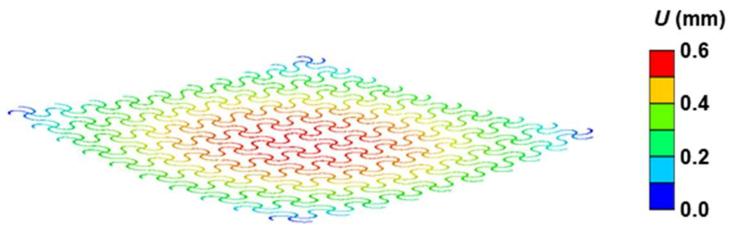

Supplementary Figure 37. Displacement contour of the metal mesh on the balloon stamp after picking up.

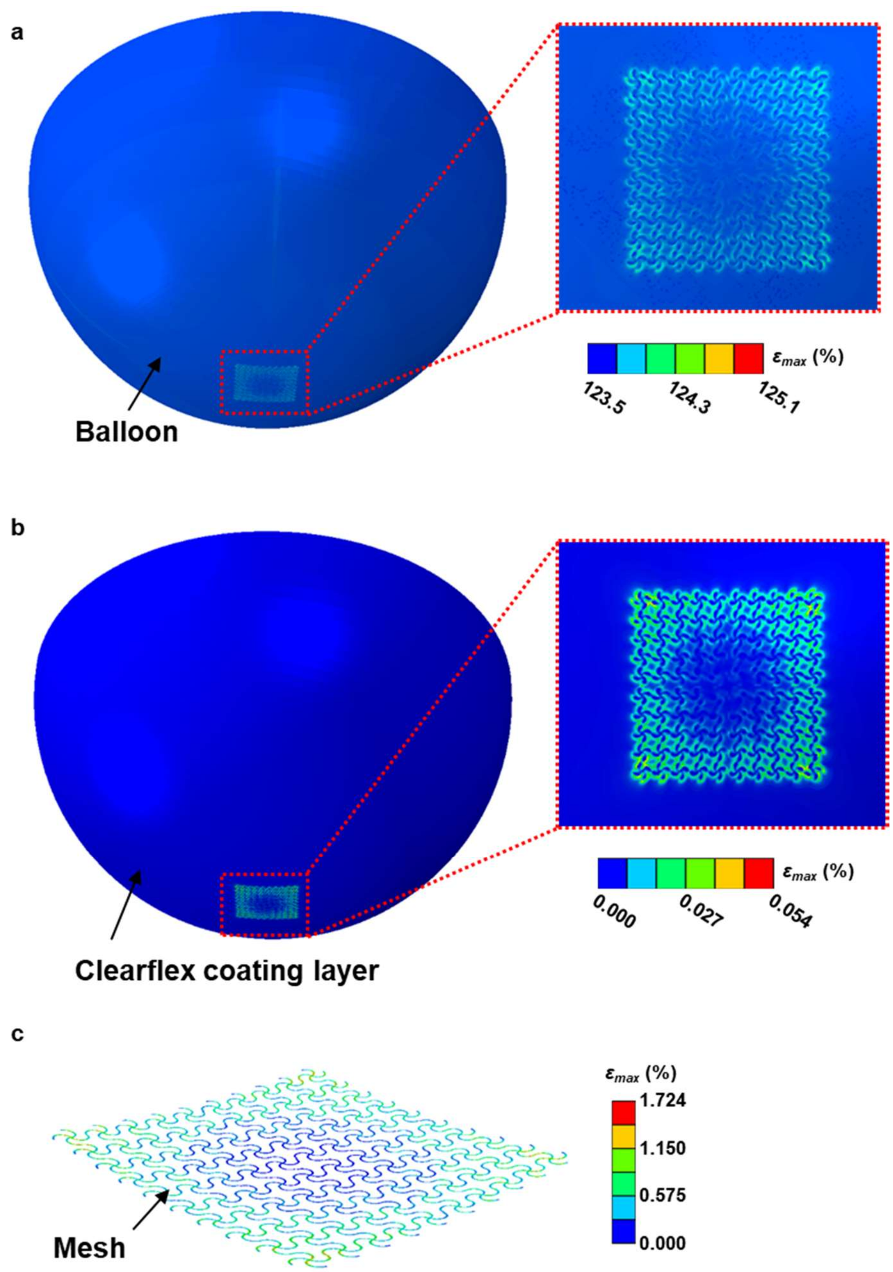

Supplementary Figure 38. Simulated strain distributions of the latex balloon (**a**), Clearflex coating layer (**b**) and the metal mesh (**c**) after picking up.

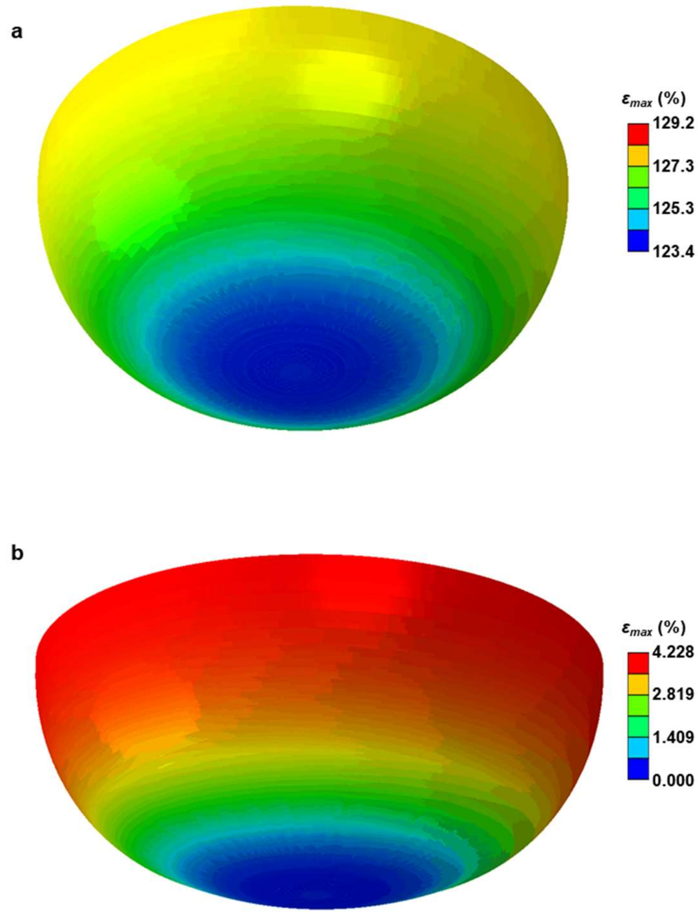

Supplementary Figure 39. Simulated strain distributions of the latex balloon (**a**) and Clearflex coating layer (**b**) during CAS printing onto the concave surface.

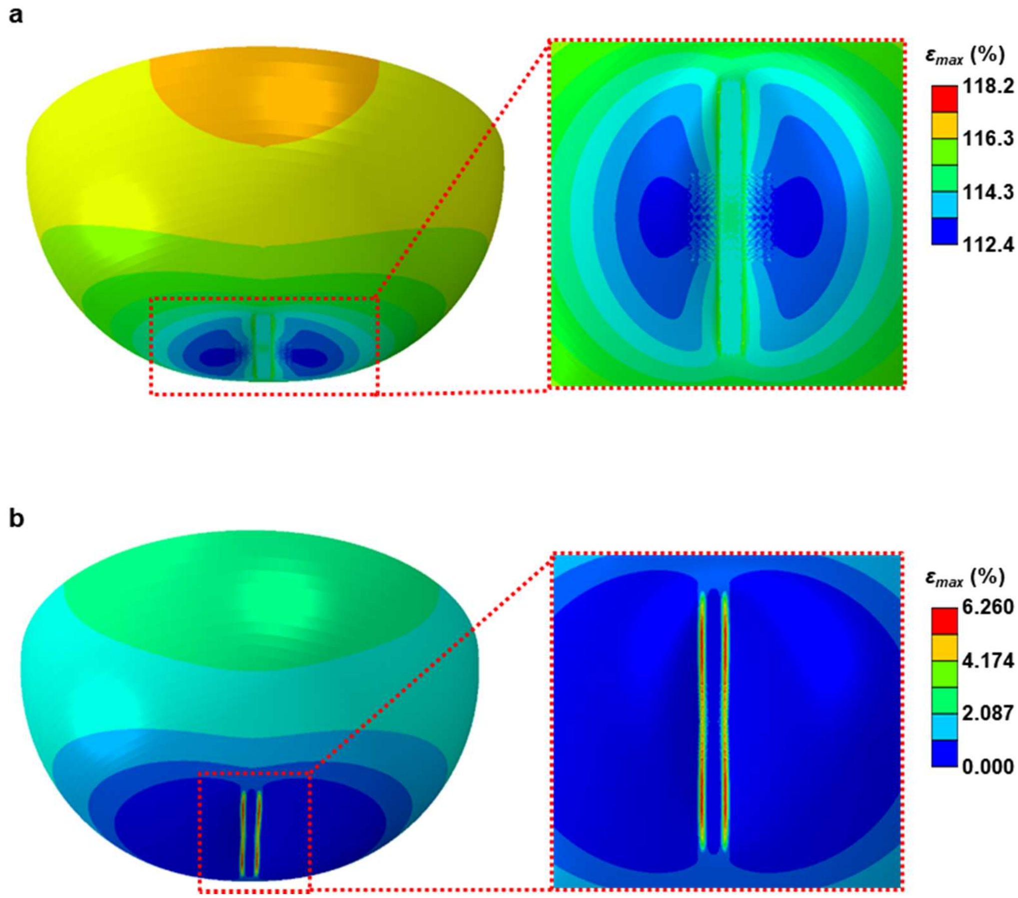

Supplementary Figure 40. Simulated strain distributions of the latex balloon (**a**) and Clearflex coating layer (**b**) during CAS printing onto the wavy surface.

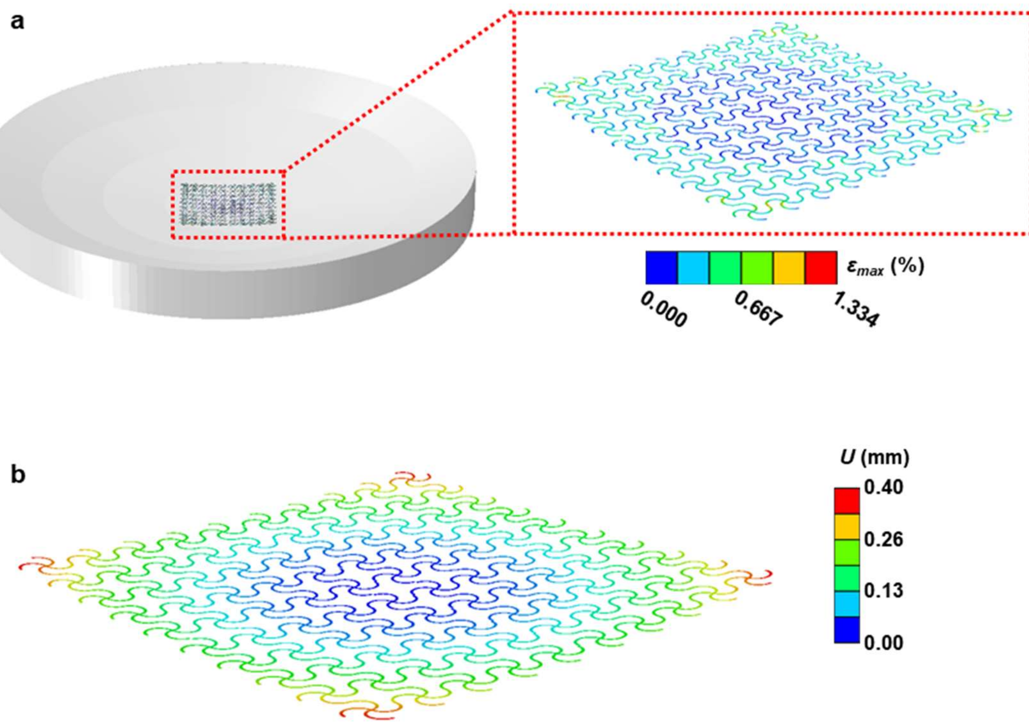

Supplementary Figure 41. Simulated strain (**a**) and displacement (**b**) contours of the metal mesh after CAS printing onto a concave substrate.

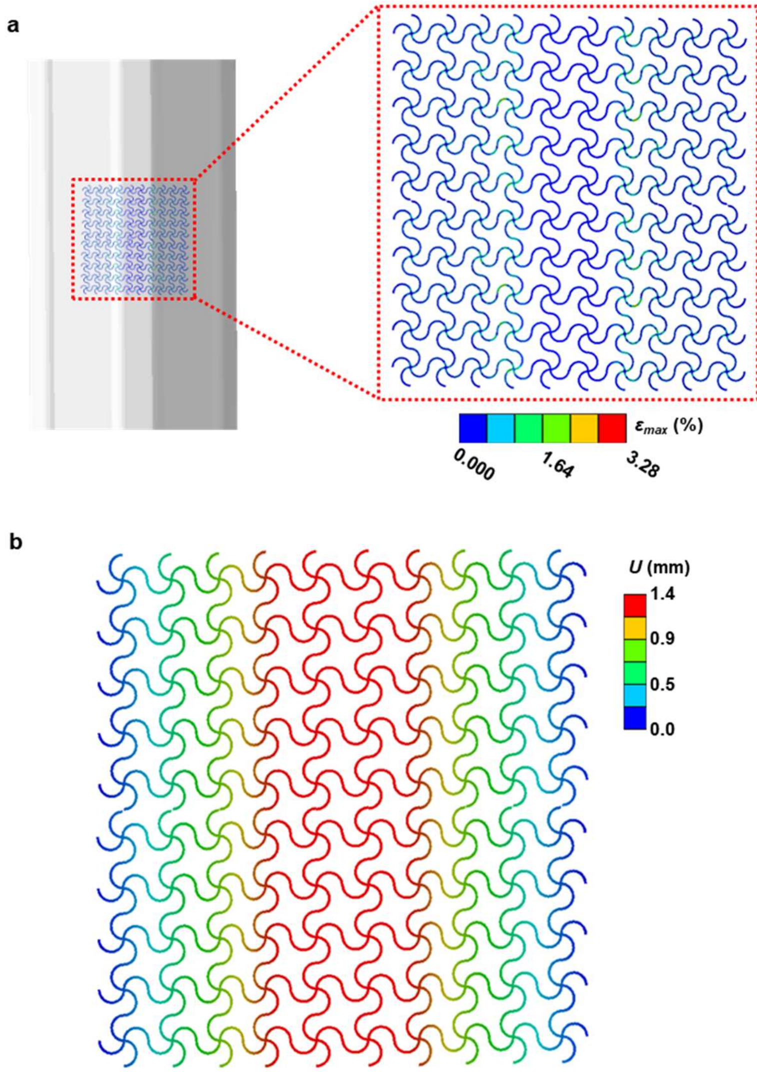

Supplementary Figure 42. Simulated strain (**a**) and displacement (**b**) contours of the metal mesh after CAS printing onto a wavy substrate.

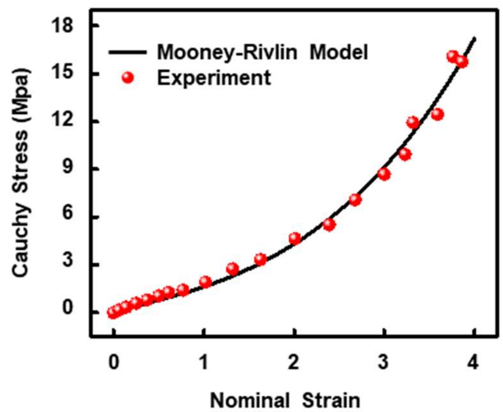

Supplementary Figure 43. The stress-strain curves of the latex balloon obtained from the experiment under equibiaxial tension and from the Mooney-Rivlin hyperelastic model.

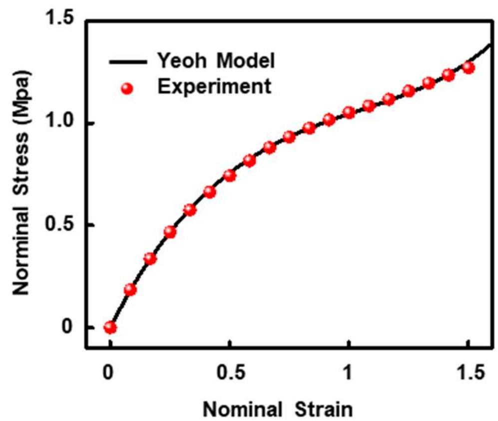

Supplementary Figure 44. The stress-strain curve for latex balloon obtained from the experiment under uniaxial tension and from the Yeoh hyperelastic model.